

Thermodynamics of partonic matter in relativistic heavy-ion collisions from a multiphase transport model

Han-Sheng Wang,¹ Guo-Liang Ma,^{1,*} Zi-Wei Lin,² and Wei-jie Fu³

¹*Key Laboratory of Nuclear Physics and Ion-beam Application (MOE),
Institute of Modern Physics, Fudan University, Shanghai 200433, China*

²*Department of Physics, East Carolina University,
C-209 Howell Science Complex, Greenville, NC 27858*

³*School of Physics, Dalian University of Technology, Dalian, 116024, China*

Using the string melting version of a multiphase transport (AMPT) model, we focus on the evolution of thermodynamic properties of the central cell of parton matter produced in Au+Au collisions ranging from 200 GeV down to 2.7 GeV. The temperature and baryon chemical potential are calculated for Au+Au collisions at different energies to locate their evolution trajectories in the QCD phase diagram. The evolution of pressure anisotropy indicates that only partial thermalization can be achieved, especially at lower energies. Through event-by-event temperature fluctuations, we present the specific heat of the partonic matter as a function of temperature and baryon chemical potential that is related to the partonic matter's approach to equilibrium.

PACS numbers:

I. INTRODUCTION

The ultrarelativistic heavy ion collisions at the BNL Relativistic Heavy Ion Collider (RHIC) and the CERN Large Hadron Collider (LHC) have created the partonic matter at extreme conditions of temperature and energy densities, the Quark-Gluon Plasma (QGP), which is governed by the Quantum Chromodynamics (QCD) theory. The first principle Lattice QCD calculation shows that the transition from hadronic to the partonic matter at zero baryon chemical potential μ_B is a smooth crossover [1–3]. But the calculation of phase transition in the QCD phase diagram at finite baryon chemical potential still has large uncertainties [4–6], especially regarding the conjectured end point of the first order phase transition boundary that is the so-called QCD critical end point (CEP) [7–9], due to the famous sign problem [10–12].

To explore the nature of the QCD phase diagram, the Beam Energy Scan (BES) program at the Relativistic Heavy-Ion Collider (RHIC) is searching for the QCD critical point with Au+Au collisions at a large range of collision energies [13–18]. The fireballs created in Au+Au collisions at different energies freeze out at different points of the QCD phase diagram. Because certain singularities will appear at the CEP in the thermodynamic limit [19], we expect to observe certain non-monotonic behaviors if the evolution trajectory of the colliding system is close enough to the CEP. For example, event-by-event fluctuations of various conserved quantities are proposed as possible signatures of the existence of the CEP [20–22] because they are proportional to the corresponding susceptibilities and correlation lengths. Many recent experimental results on net-proton fluctuations hint that a critical point might have been reached during the evolution

of Au+Au collisions at a low collision energy [14, 18, 23], which serves as a main motivation for the upcoming research projects such as those at FAIR in Germany, NICA in Russia, and HIAF in China.

Temperature and baryon chemical potential specify a thermodynamic state of the QCD matter. Meanwhile, their fluctuations are deeply related to the phase properties and phase transitions. The fluctuations of thermodynamic quantities are affected by the interactions among the constituent particles. For example, fluctuations of the temperature of thermal system provide an measure of the specific heat C_v , and the irregular behavior of specific heat is related to phase transitions. There have been many investigations on the specific heat in relativistic heavy ion collisions [24–34].

On the other hand, it is difficult to connect thermal properties of static QCD matter with the experimental measurements, since relativistic heavy-ion collisions involve many different dynamical evolution stages. To study the full evolution history of the thermodynamic properties of the QCD matter with a dynamical transport model may serve as a bridge between the gap [35, 36]. In this work, we investigate the space-time evolution of the parton matter created in Au+Au collisions at different energies, including transverse flow, effective temperature and baryon chemical potential, pressure anisotropy and specific heat by using the string melting version of a multiphase transport (AMPT) model [37].

The paper is organized as follows. Section II briefly introduces the string melting version of AMPT model and the parameters that we use. Comparison of the space-time evolution of transverse flow at different collision energies are presented in Sec. III A. We then discuss the space-time evolution of the effective temperature and baryon chemical potential in Sec. III B. We show the trajectories of Au+Au collisions at different energies in the QCD phase diagram in Sec. III C. We discuss the time evolution of pressure anisotropy in Sec. III D. The evo-

*glma@fudan.edu.cn

lution of event-by-event fluctuations of the temperature and specific heat of the partonic matter are discussed in Sec. III E. Finally, a summary is given in Sec. IV.

II. THE STRING MELTING VERSION OF A MULTIPHASE TRANSPORT MODEL

The string melting version of AMPT model consists of fluctuating initial conditions from the heavy ion jet interaction generator (HIJING) model. In this model, minijet partons and strings are produced from hard processes and soft processes, respectively. Meanwhile, all excited hadronic strings in the overlap volume are converted into partons. The interactions among these partons are described by Zhang's parton cascade (ZPC) model [38], which includes parton two-body scatterings based on the leading order pQCD $gg \rightarrow gg$ cross section:

$$\frac{d\sigma}{dt} = \frac{9\pi\alpha_s^2}{2} \left(1 + \frac{\mu^2}{s}\right) \frac{1}{(t - \mu^2)^2}. \quad (1)$$

In the above, α_s is the strong coupling constant (taken as 0.33), while s and t are the usual Mandelstam variables. The effective screening mass μ is taken as a parameter in ZPC for the parton scattering cross section, and we set μ as 2.265 fm^{-1} leading to a total cross section of about 3 mb for elastic scatterings. The AMPT model implements a simple quark coalescence model, which combines nearby freeze-out partons into mesons or baryons, to simulate the transition from the partonic matter to the hadronic matter. The final-stage hadronic evolutions are modeled by an extension of a relativistic transport model (ART) including both elastic and inelastic scatterings for baryon-baryon, baryon-meson and meson-meson interactions [39]. Our other parameters are taken as same as those from Ref. [36, 41], which can reasonably reproduce many experimental observables such as rapidity distributions, p_T spectra, and anisotropic flows [40–42] for both Au+Au collisions at RHIC and Pb+Pb collisions at LHC energies.

Using the string-melting version of the AMPT model, 10,000 events of Au+Au central collisions (0 – 5%, simulated with $b \leq 3 \text{ fm}$) are generated for each energy ($\sqrt{s_{NN}}=200, 62.4, 39, 27, 19.6, 11.5, 7.7, 4.9, \text{ and } 2.7 \text{ GeV}$) which can be provided by RHIC, FAIR and NICA facilities. We only consider the space-time evolution of the partonic matter in the parton cascade, for which necessary information is recorded and analyzed for its thermodynamics properties. In our convention, the x axis is chosen along the direction of impact parameter b from the target center to the projectile center, the z axis is along the beam direction, and the y axis is perpendicular to both x and z directions. The time t starts when the two gold nuclei are fully overlapped in the longitudinal direction, while the proper time τ is defined as $(t^2 - z^2)^{1/2}$.

III. RESULTS AND DISCUSSIONS

A. Space-time evolution of transverse flow

We first calculate the radial flow employing $\vec{\beta} = (\sum_i \vec{p}_i / \sum_i E_i)$, where the sum over index i takes into account all partons in the cell from all events of a given collision system.

Flow component β_x along the x direction as functions of coordinate x and space-time rapidity η_s at different times in cells within $0.5 < y < 0.5 \text{ fm}$ in central Au+Au collisions at $\sqrt{s_{NN}}=200 \text{ GeV}$ and 7.7 GeV are shown in Fig. 1. We can see the antisymmetry of the transverse flow along x axis at all space-time rapidity, after averaging over many events of central collisions. The flow is very small at the early time $\tau = 0.2 \text{ fm}/c$ and then develops rather fast away at large x [36].

Figure 2 shows the transverse flows of partons in the two selected cells at ($x = 3 \text{ fm}$ and $y = 0 \text{ fm}$) and ($x = 7 \text{ fm}$ and $y = 0 \text{ fm}$) within space-time rapidity $|\eta_s| < 0.5$ as functions of proper time in central Au+Au collisions at different energies. The transverse flow is bigger further away from the overlap center of central collisions [36]. We found that the transverse flow increases with the decrease of collision energy for the inner cell (at $x = 3 \text{ fm}$), but similar for the outer cell (at $x = 7 \text{ fm}$).

B. Space-time evolution of temperature and baryon chemical potential

In the AMPT model, the energy-momentum tensor can be calculated by averaging over particles and events in a volume V [35], i.e.,

$$T^{\mu\nu} = \frac{1}{V} \sum_i \frac{p_i^\mu p_i^\nu}{E_i}. \quad (2)$$

The energy density can be given by $\epsilon = T^{00}$, while the pressure components are related to the energy-momentum tensor by $P_x = T^{11}$, $P_y = T^{22}$, $P_z = T^{33}$.

For a massless quark-gluon plasma in full chemical and thermal equilibrium as given by the Bose-Einstein and Fermi-Dirac distributions, the energy density and temperature T obey the following relation:

$$\epsilon = d_{QGP} \frac{\pi^2}{30} T^4, \quad (3)$$

where $d_{QGP} = d_g + 7d_q/8 = 16 + 10.5N_f$ is the total degeneracy factor of the QGP, and N_f represents the number of relevant quark flavors ($N_f = 3$ is considered in our investigation). With the above assumption, we can calculate the temperature [36] and baryon chemical potential [44] according to

$$T = \sqrt[4]{\frac{30}{d_{QGP}\pi^2}\epsilon}, \quad (4)$$

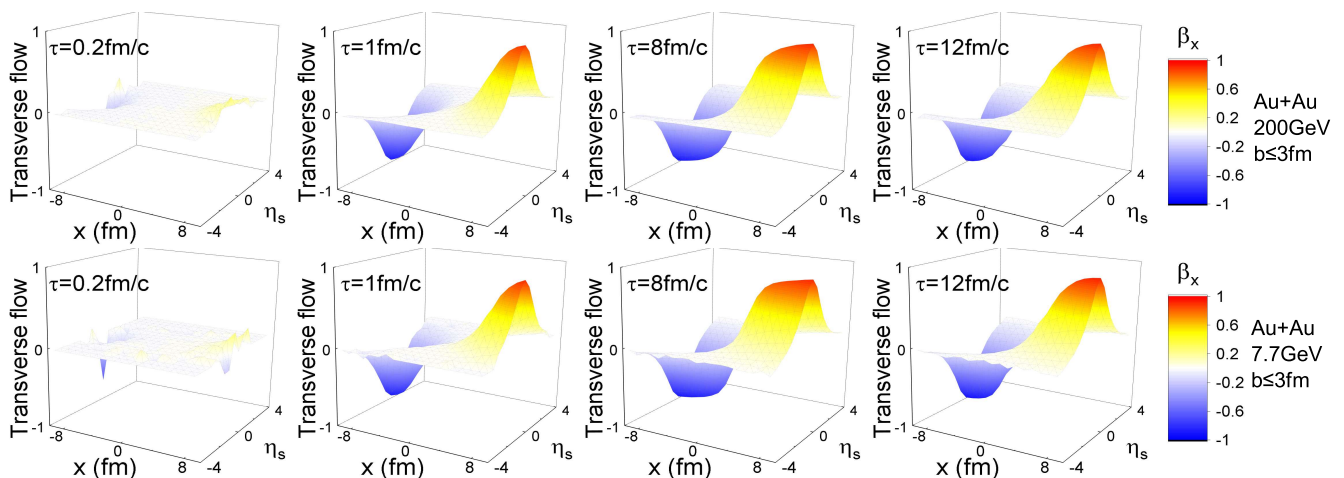


FIG. 1: (Color online) Transverse flow component β_x along the x axis ($0.5 < y < 0.5$ fm) as functions of x and η_s at different proper times in central Au+Au collisions at $\sqrt{s_{NN}}=200$ GeV (first row) and 7.7 GeV (second row).

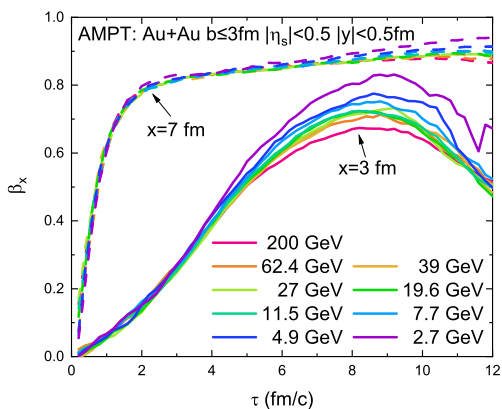


FIG. 2: (Color online) Proper time evolution of transverse flow component β_x of partons within space-time rapidity $|\eta_s| < 0.5$ in the cells at $(x,y)=(3 \text{ fm}, 0 \text{ fm})$ (solid curve) and $(x,y)=(7 \text{ fm}, 0 \text{ fm})$ (dash curve) in central Au+Au collisions at different energies.

$$\mu_B = (5n_B - n_Q + 2n_S)/T^2, \quad (5)$$

where $n_{B,Q,S}$ are the density of net baryon, net electric charge, and net strangeness, respectively. Note that Eq. (5) holds for a non-interacting massless parton system with a small chemical potential in principle. The energy density in the rest frame of a cell should be used to obtain the local effective temperature in order to remove the effect of radial flow. However, the central cell that we consider here is special because it is always at rest. Also note that, since partons in the cell may not be in full thermal and chemical equilibrium [36] (which will be discussed in Sec. III D), these extracted temperature

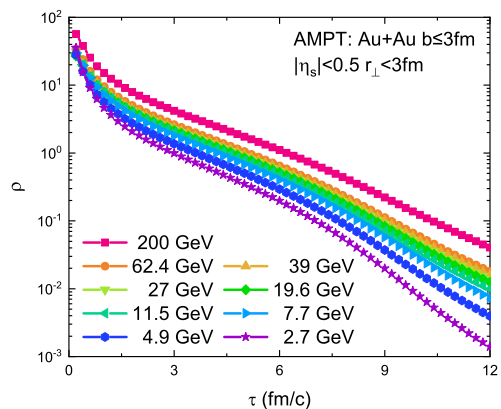


FIG. 3: (Color online) Proper time evolution of the parton density in the central cell ($r_{\perp} < 3$ fm) within space-time rapidity $|\eta_s| < 0.5$ in central Au+Au collisions at different energies.

and baryon chemical potential are the effective values.

Figure 3 shows the densities of partons at the center of fireball ($r_{\perp} < 3$ fm) within space-time rapidity $|\eta_s| < 0.5$ as functions of proper time in central Au+Au collisions at different energies. The density decreases with the proper time, with the decrease being slower at higher collision energies because more parton collisions can better maintain the density of the fireball.

The 2D distributions of local effective temperature as functions of coordinate x and space-time rapidity at different proper times in central Au+Au collisions at $\sqrt{s_{NN}}=200$ and 7.7 GeV are shown in Fig. 4. We can see that the highest temperature is reached in the early time at the center of the overlap region, and the temperature decreases with the expansion and evolution of the

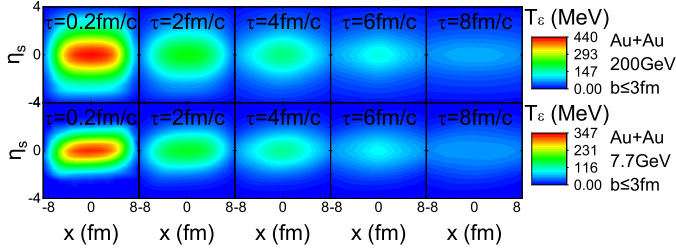


FIG. 4: (Color online) Contour plots of effective temperature as a function of x coordinate and space-time rapidity η_s at different proper times in central Au+Au collisions at $\sqrt{s_{NN}} = 200$ GeV (first row) and 7.7 GeV (second row), where y coordinate is chosen within $|y| < 0.5$ fm.

system.

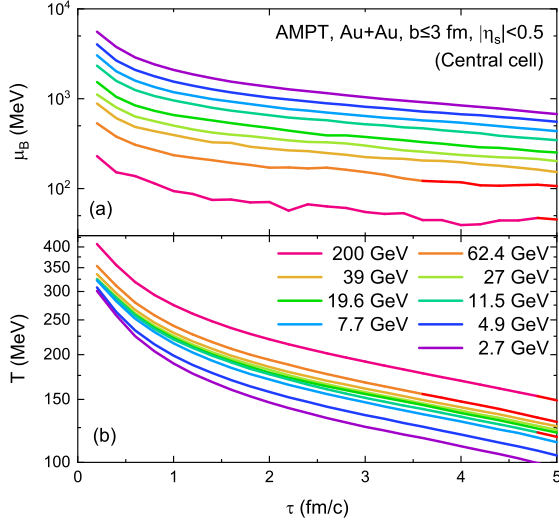


FIG. 5: (Color online) Proper time evolution of baryon chemical potential (a) and temperature (b) of the central cell within space-time rapidity $|\eta_s| < 0.5$ in central Au+Au collisions at different energies.

The proper time evolutions of the baryon chemical potential and temperature for the central cell within the space-time rapidity range of $-0.5 < \eta_s < 0.5$ in central Au+Au collisions at different beam energies from the AMPT-SM model are shown in Fig. 5(a) and (b), respectively. We can see that both baryon chemical potential and temperature decrease with time, which indicates that the collision system tends to be more dilute and cool down due to the expansion. However, the energy dependences of the baryon chemical potential and temperature are totally different. As is well known, higher temperatures are reached at higher collision energies, but higher baryon chemical potentials are achieved at lower collision energies.

Since baryon chemical potential consists of three components as shown in Eq.(5), Fig. 6 (a) and (b) show the

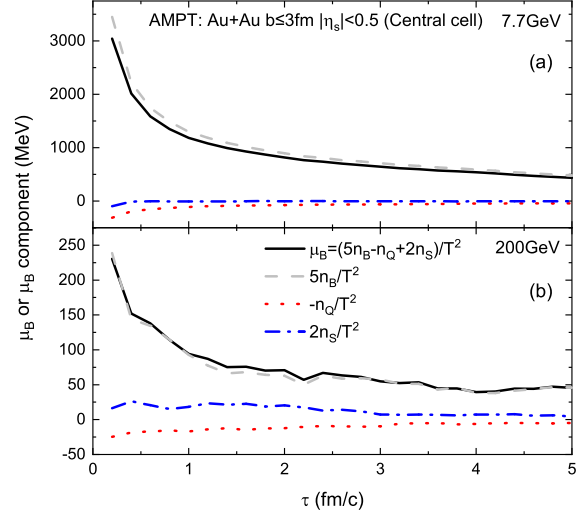


FIG. 6: (Color online) Proper time evolution of components of baryon chemical potential of the central cell within space-time rapidity $|\eta_s| < 0.5$ in central Au+Au collisions at 7.7 (a) and 200 (b) GeV.

proper time evolution of the three components of baryon chemical potential $[(5n_B)/T^2, (-n_Q)/T^2, (2n_S)/T^2]$ of the central cell in central Au+Au collisions at 7.7 and 200 GeV, respectively. We can see that the baryon chemical potential is dominated by the net baryon number density. We also find that the total baryon chemical potential is slightly lower than the component from the net baryon number density in Au+Au collisions at 7.7 GeV while it is often the opposite at 200 GeV; this is mainly due to the increase of the relative contribution from the net strangeness number density at the higher colliding energy.

C. Trajectories in the QCD phase diagram

In Fig. 7 we present the event-averaged evolution trajectory of the central cell of the partonic matter produced in central Au+Au collisions at different beam energies from the time of 1 fm/c to the moment when it reaches the crossover curve in the temperature and baryon chemical potential diagram. Note that the crossover phase boundary is obtained from the functional renormalisation group (FRG) method with $N_f = 2 + 1$, which well agrees with the phase boundary from the Lattice QCD[6]. It is interesting to find that the durations of the partonic stage are around 4 fm/c, which is consistent with the previous AMPT results for mid-central Au+Au collisions [45]. If we take the location of the critical end point at $(T_{CEP}, \mu_{BCEP}) = (107, 635)$ MeV from the FRG calculation, the beam energies between 2.7 and 4.9 GeV [6, 48] seem to be the most promising to reach the CEP, which could be accessed at fixed target experiments at RHIC or in

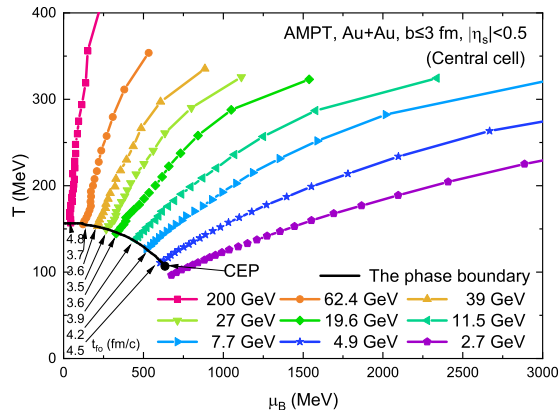


FIG. 7: (Color online) AMPT results on the average trajectory of the central cell in central Au+Au collisions at different energies in the QCD phase diagram of temperature versus baryon chemical potential. The black curve shows the crossover phase boundary with the critical end point obtained from the functional renormalisation group approach with $N_f = 2 + 1$ [6]. The time values at which each trajectory intersects the phase boundary are also shown.

the future. Note that it has been found that the chemical and kinetic freeze-out parameters extracted from the AMPT model agree with the RHIC experimental measurements [49].

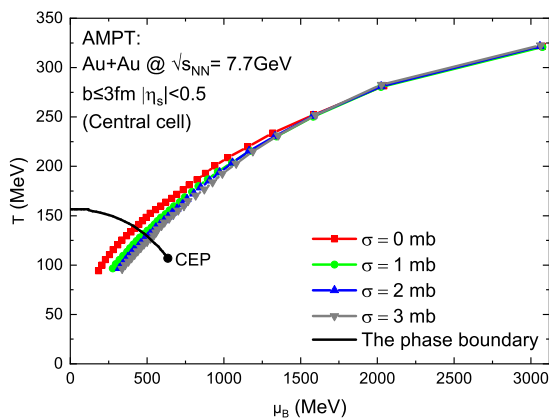


FIG. 8: (Color online) AMPT results on the average trajectory of the central cell in central Au+Au collisions at 7.7 GeV at different parton cross sections in the QCD phase diagram of temperature versus baryon chemical potential.

We also investigate the effect of parton cross section on the event-averaged trajectory in the QCD phase diagram for Au+Au collisions at 7.7 GeV, since different interaction strength can affect the evolution of the collision system. In Fig. 8, we can see that a larger cross section pushes the evolution trajectory downward; consequently the intersection point is closer to the CEP with

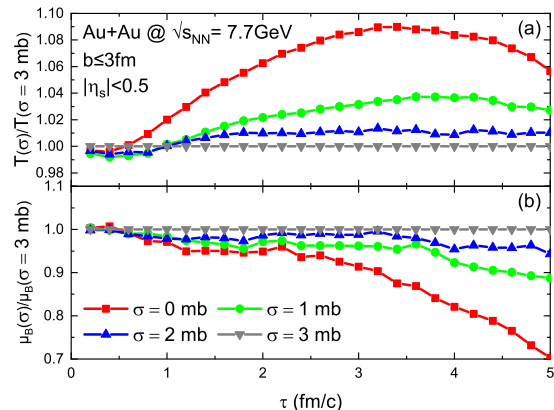


FIG. 9: (Color online) Time evolution of the ratios of temperature (a) and baryon chemical potential (b) at a given parton cross section over that at 3mb cross section for central Au+Au collisions at 7.7 GeV.

a larger parton cross section for Au+Au collisions at 7.7 GeV. More details can be seen in Fig. 9, which shows the time evolution of the ratios of temperature or baryon chemical potential at each parton cross section over that at 3mb. We can see that the decrease of temperature is slower with a smaller cross section, but the opposite is true for the baryon chemical potential.

We note that the string melting version of the AMPT model that we use in this study does not include the finite nuclear thickness, which effect could be important for heavy ion collisions at low energies. For example, it has been found [46, 47] that at low energies the finite nuclear thickness along the beam direction leads to a lower peak value but a longer evolution time for the produced initial energy density. This would affect the time evolution of the effective temperature and consequently the evolution trajectory of heavy ion collisions at the BES energies and below. Further studies that includes the finite nuclear thickness are warranted.

We should point out that the above results come from the average of 10,000 central Au+Au events. However, event-by-event fluctuations can not be neglected, and these fluctuations could affect the search for the CEP of the QCD phase diagram. Figure 10 shows the event-by-event trajectories of central Au+Au collisions at different beam energies from the AMPT-SM model, where the black curve in each panel represents the phase transition crossover boundary from FRG [6]. To suppress the effect from multiplicity or volume fluctuation, a multiplicity cut is further applied, where we divide the total events into 100 bins by multiplicity and only use the events in one middle bin around the average. Even so, we can see that the fluctuation is quite large, especially at high energies. From the initial state to the late stage, these trajectories are distributed in a wide area around the averaged trajectory; this is consistent with the recent hydrodynamical result [50]. It is interesting to see that some trajectories

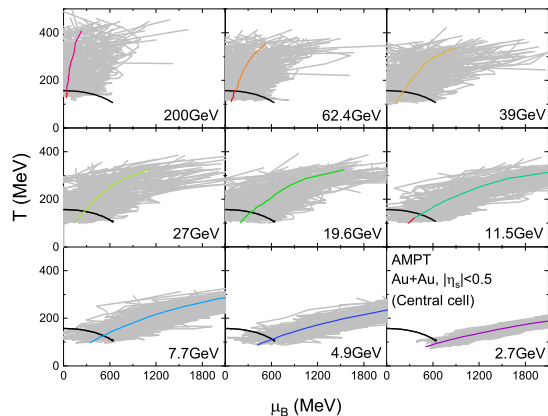


FIG. 10: (Color online) AMPT results on event-by-event trajectories of the central cell in central Au+Au collisions at different beam energies in the QCD phase diagram of temperature versus baryon chemical potential.

can pass the CEP because of event-by-event fluctuations, which could further lead to possible critical behaviors.

D. Pressure anisotropy

In the central cell of central Au+Au collisions, due to the cylindrical symmetry around the beam axis, the two transverse pressure components P_x and P_y are equal. Therefore, the transverse pressure can be defined to be $P_T = (P_x + P_y)/2$ [35], while the longitudinal pressure P_L is just P_z . For a system in thermal equilibrium, its pressure must be isotropic, which satisfies the relation of $P_T = P_L = P$. Therefore, a pressure anisotropy parameter, P_L/P_T , is defined to describe the degree of pressure anisotropy of the system in thermal equilibrium. The closer the value of P_L/P_T is to unity, the closer the system to the state of thermal equilibrium.

Figure 11 shows how the pressure anisotropy parameter of partons in the central cell evolves with proper time in central Au+Au collisions at different beam energies. We see that P_L/P_T keeps increasing up to 5 fm/c in Au+Au collisions at 200 GeV; however, it still does not reach unity. It indicates that even for the top RHIC energy the central cell of the system actually does not reach thermal equilibrium when it arrives at the phase boundary in the AMPT model, consistent with the previous result [36]. For lower energies, P_L/P_T increases at early times but saturates around 0.7 at late times. For the lowest energy of 2.7 GeV, P_L/P_T first increases and then gradually decreases with time.

In order to understand why the AMPT model shows the above time evolution of the pressure anisotropy parameter, Fig. 12 presents the average number of collisions of each parton per unit proper time for the central cell in central Au+Au collisions at different beam en-

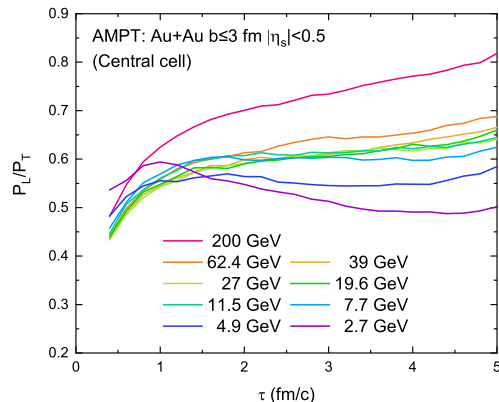


FIG. 11: (Color online) AMPT results on the time evolution of the pressure anisotropy parameter of partons in the central cell in central Au+Au collisions at different beam energies.

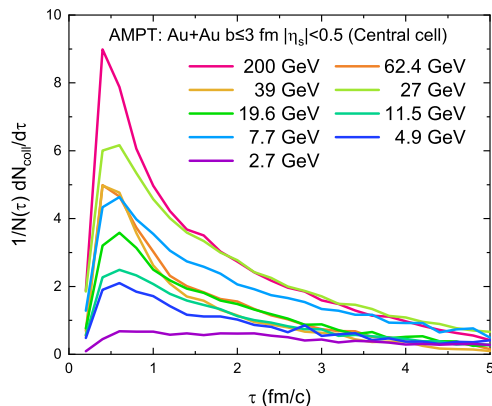


FIG. 12: (Color online) AMPT results on the average number of collisions of each parton per unit proper time as a function of the proper time for the central cell in central Au+Au collisions at different beam energies.

ergies. We see that the partons have few collisions at early times since most partons have not been formed, and then they collide most frequently around 0.5 fm/c. For higher beam energies, they can keep colliding until the phase boundary (~ 4 fm/c), which helps to increase the pressure anisotropy parameter towards thermal equilibrium. However, fewer collisions happen at late times due to the expansion, which make the progress towards thermal equilibrium incomplete when the system reaches the QCD phase boundary [51]. We should also emphasize that, since the parton systems of Au+Au collisions at different energies from the AMPT model are not in complete equilibrium [35, 43], the thermodynamic properties we extracted here are only approximate.

E. Temperature fluctuations and specific heat

Thermodynamic quantities always fluctuate around their thermal averages, because the entropy is required to reach its maximum in equilibrium. By taking advantage of thermodynamic fluctuations, we can learn more about thermal properties of an equilibrium system. For instance, the event-by-event temperature fluctuation of an equilibrium system obeys the probability distribution [24]:

$$P(T) \sim \exp\left[-\frac{C_v}{2} \frac{(\Delta T)^2}{\langle T \rangle^2}\right], \quad (6)$$

where $\langle T \rangle$ is the mean temperature and $(\Delta T)^2 = (T - \langle T \rangle)^2$ is the variance in temperature [19]. For a Gaussian fluctuation, the specific heat can be easily obtained as [27]

$$\frac{1}{C_v} = \frac{(\Delta T)^2}{\langle T \rangle^2}. \quad (7)$$

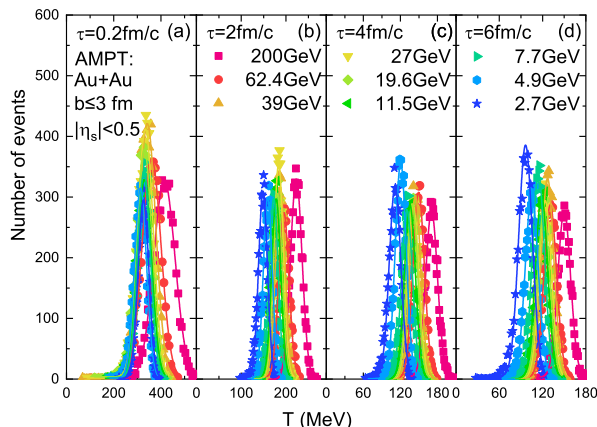


FIG. 13: (Color online) AMPT results on the event-by-event effective temperature distributions of partons for the central cell within $|\eta_s| < 0.5$ for (a) $\tau = 0.2$ fm/c, (b) $\tau = 2$ fm/c, (c) $\tau = 4$ fm/c, and (d) $\tau = 6$ fm/c in central Au+Au collisions at different beam energies, where symbols and curves represent the AMPT results and Gaussian fits, respectively.

The AMPT results on the event-by-event effective temperature distributions for the partons in the central cell (within $|\eta_s| < 0.5$) at different proper times in central Au+Au collisions at different beam energies are shown in Fig. 13, where the symbols and curves represent the AMPT results and Gaussian fits, respectively. Thus we can extract the widths of the temperature distributions, which are shown in Fig. 14 as functions of the proper time for the central cell in central Au+Au collisions at different energies. We can see that the width decreases with time, which means the fluctuation of temperature is reduced with time during the expansion and parton

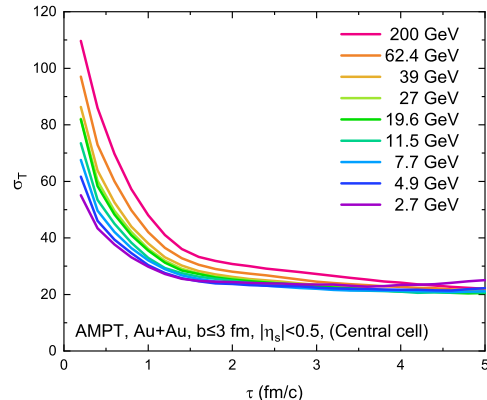


FIG. 14: (Color online) AMPT results on the time evolution of the width of the temperature distribution of partons in the central cell in central Au+Au collisions at different energies.

cascade. Although collisions at higher collision energies have a larger temperature fluctuation at the beginning, they reach similar fluctuations at late times.

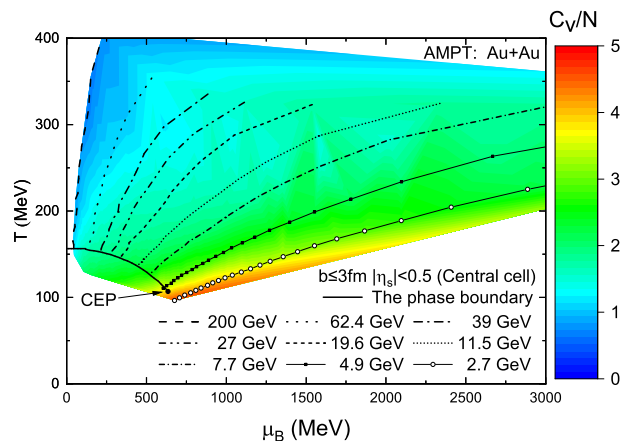


FIG. 15: (Color online) AMPT results on the specific heat per parton, C_v/N , of the central cell in central Au+Au collisions as a function of baryon chemical potential and temperature, where the average evolution trajectories of the central cell and the crossover phase boundary with the critical end point are also shown.

Based on Eq. (7), the specific heat of the central cell of the partonic matter can be extracted. Since the specific heat, as an extensive quantity, reflects the total energy per unit of temperature change needed by all partons in the cell, we introduce a normalized specific heat C_v/N , where N is the parton multiplicity in the central cell. Figure 15 shows the normalized specific heat as functions of baryon chemical potential and temperature for partons in the central cell in central Au+Au collisions from the AMPT model. We find that the normalized specific heat increases with the decrease of temperature and the in-

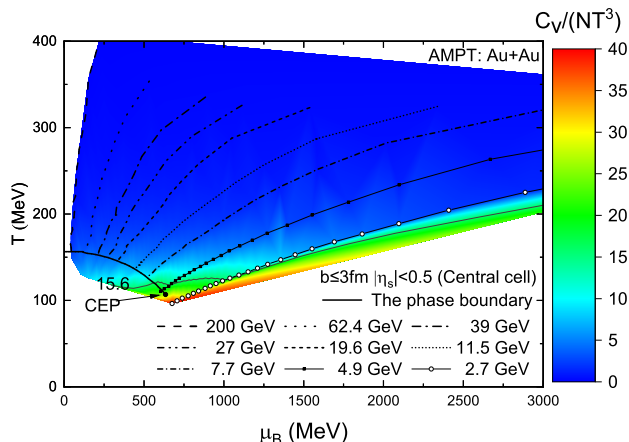


FIG. 16: (Color online) AMPT results on the dimensionless specific heat per parton, $C_v/(NT^3)$, of the central cell in central Au+Au collisions as a function of baryon chemical potential and temperature, where the average evolution trajectories of the central cell and the crossover phase boundary with the critical end point and the line for 15.6 are also shown.

crease of baryon chemical potential in general. It also reaches a maximum around the CEP within the energy ranges shown in the figure. Compared to preliminary results from the RHIC-STAR experiment [34], however, our result is systematically lower than the experimental data for lower energies. But it should be noticed that our specific heat is aimed at the evolution of partonic matter, however the experimental results are obtained based on the information from final freeze out hadrons.

Since we assume that the partonic matter is a massless quark-gluon plasma in full chemical and thermal equilibrium in extracting the effective temperature, $C_v/(NT^3)$ should be a dimensionless constant of $d_{QGP}\pi^2/30 \sim 15.6$ by definition. Figure 16 shows the dimensionless specific heat per parton, $C_v/(NT^3)$, of the central cell in central Au+Au collisions as a function of baryon chemical potential and temperature. We can see that it increases from a small value in the early time of Au+Au collisions to a large value along the trajectory, close to the expected value of ~ 15.6 around the phase boundary at certain low energies. It indicates that the partonic matter goes from a far-from-equilibrium state to a state closer to thermal equilibrium, where the relation between the specific heat and temperature fluctuation holds approximately. The deviations from the expected $C_v/(NT^3)$ value could result from dynamical fluctuations or the non-equilibrium evolution of partonic matter.

IV. SUMMARY

We have studied the space-time evolution of the parton matter produced in 0-5% most central Au+Au collisions at different collision energies using the AMPT model with string melting. We extract the effective tempera-

ture and baryon chemical potential of the partons in the central cell. The temperature and baryon chemical potential both decrease with time, but their dependences on the collision energy are opposite. By investigating the evolution of the partonic matter created in Au+Au collisions at different energies, we obtain their trajectories in the QCD phase diagram. The results indicate that the partonic state exists until about 4 fm/c, and the CEP proposed by the FRG approach is located between the trajectories at the collision energies of 2.7 and 4.9 GeV. We find that the parton interaction cross section influences the evolution trajectory of the collision system and the trajectory also fluctuates event-by-event. These features could be important for the experimental search for the CEP. By studying pressure anisotropies in 0-5% most central Au+Au collisions at different collision energies, we find that the parton matter from the AMPT model is still in incomplete thermal equilibrium in the region near the QCD phase boundary. We also use temperature fluctuations to investigate the evolution of the specific heat of the partonic matter in the AMPT model. We find that the dimensionless specific heat per parton increases with time and gets closer to the expected value near the QCD phase boundary, indicating that the partonic system gets closer to thermal equilibrium.

It should be noted that the AMPT model currently only includes two-body elastic parton collisions with a leading-order pQCD gluon elastic scattering cross section, which is controlled by a Debye screening mass. However, it has been demonstrated that the pQCD $gg \leftrightarrow ggg$ bremsstrahlung processes can isotropize momentum more efficiently than elastic scatterings [52]. In addition, the QGP created in high energy heavy-ion collisions, which may consist of gluons and quarks in or near chemical and thermal equilibrium, should be governed by non-perturbative QCD interactions. Furthermore, the method that we used to extract temperature and baryon chemical potential works for non-interacting massless parton system with a small chemical potential in principle, and we have not include the effect of finite nuclear thickness that has been shown to be important at low energies. Due to these limitations, we expect that our calculations can only provide qualitative features of the non-equilibrium dynamical evolution. In addition, we have focused on the central space-time rapidity and only studied the partonic matter without the subsequent phase transition and hadronic evolution. Further studies of the evolution and the thermodynamic properties of the matter in heavy-ion collisions are indispensable for studying the QCD phase structure and the experimental search for the critical point.

Acknowledgments

This work is supported in part by the Strategic Priority Research Program of Chinese Academy of Sciences under Grant No. XDB34030000, the National Natural Science

Foundation of China under Contracts No. 11961131011, No. 11890710, No. 11890714, No. 11835002, and the Guangdong Major Project of Basic and Applied Basic Research under Grant No. 2020B0301030008 (H.-L. W.

and G.-L.M.), National Science Foundation under Grant No. 2012947 (Z.-W.L.), and National Natural Science Foundation of China under Contract No. 11775041 (W.-j. F.).

-
- [1] Y. Aoki, G. Endrodi, Z. Fodor, S. D. Katz and K. K. Szabo, *Nature* **443**, 675 (2006)
- [2] R. Bellwied, S. Borsanyi, Z. Fodor, J. Günther, S. D. Katz, C. Ratti and K. K. Szabo, *Phys. Lett. B* **751**, 559 (2015)
- [3] A. Bazavov *et al.* [HotQCD Collaboration], *Phys. Lett. B* **795**, 15 (2019)
- [4] C. S. Fischer, J. Luecker and C. A. Welzbacher, *Phys. Rev. D* **90**, no. 3, 034022 (2014)
- [5] F. Gao, J. Chen, Y. X. Liu, S. X. Qin, C. D. Roberts and S. M. Schmidt, *Phys. Rev. D* **93**, no. 9, 094019 (2016)
- [6] W. j. Fu, J. M. Pawłowski and F. Rennecke, *Phys. Rev. D* **101**, no. 5, 054032 (2020)
- [7] R. V. Gavai and S. Gupta, *Phys. Rev. D* **78**, 114503 (2008)
- [8] M. A. Stephanov, *Prog. Theor. Phys. Suppl.* **153**, 139 (2004) [*Int. J. Mod. Phys. A* **20**, 4387 (2005)]
- [9] B. Mohanty, *Nucl. Phys. A* **830**, 899C (2009)
- [10] R. V. Gavai and S. Gupta, *Phys. Rev. D* **68**, 034506 (2003)
- [11] P. de Forcrand and O. Philipsen, *Nucl. Phys. B* **642**, 290 (2002)
- [12] Z. Fodor and S. D. Katz, *Phys. Lett. B* **534**, 87 (2002)
- [13] M. M. Aggarwal *et al.* [STAR Collaboration], *Phys. Rev. Lett.* **105**, 022302 (2010)
- [14] L. Adamczyk *et al.* [STAR Collaboration], *Phys. Rev. Lett.* **112**, 032302 (2014)
- [15] L. Adamczyk *et al.* [STAR Collaboration], *Phys. Rev. Lett.* **113**, 092301 (2014)
- [16] A. Adare *et al.* [PHENIX Collaboration], *Phys. Rev. C* **93**, no. 1, 011901 (2016)
- [17] L. Adamczyk *et al.* [STAR Collaboration], *Phys. Lett. B* **785**, 551 (2018)
- [18] J. Adam *et al.* [STAR Collaboration], arXiv:2001.02852 [nucl-ex].
- [19] L.D. Landau and I.M. Lifschitz, *Course of Theoretical Physics, Statistical Physics Vol. 5* (Pergamon Press, New York, 1958).
- [20] V. Koch, A. Majumder and J. Randrup, *Phys. Rev. Lett.* **95**, 182301 (2005)
- [21] M. Asakawa, U. W. Heinz and B. Muller, *Phys. Rev. Lett.* **85**, 2072 (2000)
- [22] M. Asakawa, S. Ejiri and M. Kitazawa, *Phys. Rev. Lett.* **103**, 262301 (2009)
- [23] X. Luo and N. Xu, *Nucl. Sci. Tech.* **28**, no. 8, 112 (2017)
- [24] L. Stodolsky, *Phys. Rev. Lett.* **75**, 1044 (1995).
- [25] E. V. Shuryak, *Phys. Lett. B* **423**, 9 (1998)
- [26] S. Chatterjee, R. M. Godbole and S. Gupta, *Phys. Rev. C* **81**, 044907 (2010)
- [27] Y. G. Ma *et al.*, *J. Phys. G* **31**, S1179 (2005)
- [28] B. H. Sa, X. M. Li, S. Y. Hu, S. P. Li, J. Feng and D. M. Zhou, *Phys. Rev. C* **75**, 054912 (2007).
- [29] A. Mekjian, *Phys. Rev. C* **73**, 014901 (2006).
- [30] R. V. Gavai, S. Gupta and S. Mukherjee, *Phys. Rev. D* **71**, 074013 (2005)
- [31] S. A. Voloshin, V. Koch and H. G. Ritter, *Phys. Rev. C* **60**, 024901 (1999)
- [32] W. Broniowski, B. Hiller, W. Florkowski and P. Bozek, *Phys. Lett. B* **635**, 290 (2006)
- [33] P. Bozek and W. Broniowski, *Phys. Rev. C* **85**, 044910 (2012)
- [34] S. Basu, S. Chatterjee, R. Chatterjee, T. K. Nayak and B. K. Nandi, *Phys. Rev. C* **94**, no. 4, 044901 (2016)
- [35] B. Zhang, L. W. Chen and C. M. Ko, *J. Phys. G* **35**, 065103 (2008)
- [36] Z. W. Lin, *Phys. Rev. C* **90**, no. 1, 014904 (2014)
- [37] Z. W. Lin, C. M. Ko, B. A. Li, B. Zhang and S. Pal, *Phys. Rev. C* **72**, 064901 (2005)
- [38] B. Zhang, *Comput. Phys. Commun.* **109**, 193 (1998)
- [39] B. A. Li and C. M. Ko, *Phys. Rev. C* **52**, 2037 (1995)
- [40] Z. W. Lin and C. M. Ko, *Phys. Rev. C* **65**, 034904 (2002)
- [41] G. L. Ma and Z. W. Lin, *Phys. Rev. C* **93**, no. 5, 054911 (2016)
- [42] L. W. Chen, C. M. Ko and Z. W. Lin, *Phys. Rev. C* **69**, 031901 (2004)
- [43] B. Zhang, *Nucl. Phys. A* **834**, 279C (2010) doi:10.1016/j.nuclphysa.2009.12.059 [arXiv:0909.0780 [nucl-th]].
- [44] A. Monnai, B. Schenke and C. Shen, *Phys. Rev. C* **100**, no. 2, 024907 (2019)
- [45] L. W. Chen, C. M. Ko, W. Liu and B. W. Zhang, *PoS CPOD 2009*, 034 (2009)
- [46] Z. W. Lin, *Phys. Rev. C* **98**, no. 3, 034908 (2018)
- [47] T. Mendenhall and Z. W. Lin, arXiv:2012.13825 [nucl-th].
- [48] A. Andronic, P. Braun-Munzinger, K. Redlich and J. Stachel, *Nature* **561**, no. 7723, 321 (2018)
- [49] D. F. Wang, S. Zhang and Y. G. Ma, *Phys. Rev. C* **101**, no. 3, 034906 (2020)
- [50] C. Shen, *Nucl. Phys. A* **1005**, 121788 (2021)
- [51] D. Bazow, G. S. Denicol, U. Heinz, M. Martinez and J. Noronha, *Phys. Rev. Lett.* **116**, no. 2, 022301 (2016)
- [52] Z. Xu and C. Greiner, *Phys. Rev. C* **76**, 024911 (2007)